ACCSCIENCE PUBLISHING

Materials Science in Additive Manufacturing

ORIGINAL RESEARCH ARTICLE

Preparation of porous magnesium alloy scaffolds with high formation quality and dimensional accuracy through contour scan optimization in laser powder bed fusion

Zeyu Feng[1], Hao Zheng[1], Baoxue Zhou[1], Bozun Miao[1], Penghuai Fu[1], Deli Wang[2], Hua Huang[1]*, and Guangyin Yuan[1,2]*

[1]National Engineering Research Center of Light Alloy Net Forming and Key State Laboratory of Metal Matrix Composites, School of Materials Science and Engineering, Shanghai Jiao Tong University, Shanghai 200240, China

[2]National and Local Joint Engineering Research Center of Orthopaedic Biomaterials, Peking University Shenzhen Hospital, Shenzhen, Guangdong 518036, China

Abstract

Biodegradable magnesium-based scaffolds for bone tissue engineering are considered a promising treatment approach for repairing large bone defects. In this study, porous magnesium-neodymium-zinc-zirconium alloy (JDBM) scaffolds were fabricated using laser powder bed fusion (L-PBF) followed by dynamic electrochemical polishing. The effects of laser energy input and contour scan strategy on the formation quality of L-PBF scaffolds were systematically investigated. A novel scanning strategy, C64F84, combining low laser power for contour scans with high laser power for filling scans, was developed to achieve good fusion quality while controlling surface powder adhesion and dross defects. The printed specimens achieved a maximum relative density of 99.54%. The effects of electrochemical polishing on L-PBF scaffolds with different contour scan strategies were further evaluated. Electrochemical polishing effectively removed excess adhered powder and brought the scaffold porosity in line with the intended design value. The polished C64F84 scaffold exhibited higher dimensional accuracy, with smaller mean deviations, due to improved geometric consistency in the L-PBF process. Finite element analysis results were consistent with compression test data, confirming the high quality of the prepared C64F84 scaffolds. The yield strength (23.88 MPa) and elastic modulus (0.855 GPa) were comparable to those of cancellous bone, highlighting the medical potential of L-PBF-fabricated JDBM scaffolds.

Keywords: Magnesium alloy scaffolds; Laser powder bed fusion; Formation quality; Dimensional accuracy; Finite element analysis

***Corresponding authors:**
Hua Huang
(huangh@sjtu.edu.cn)
Guangyin Yuan
(gyyuan@sjtu.edu.cn)

Citation: Feng Z, Zheng H, Zhou B, *et al*. Preparation of porous magnesium alloy scaffolds with high formation quality and dimensional accuracy through contour scan optimization in laser powder bed fusion. *Mater Sci Add Manuf.* 2026;5(1):025350080. doi: 10.36922/MSAM025350080

Received: August 26, 2025

Revised: September 17, 2025

Accepted: September 26, 2025

Published online: October 30, 2025

1. Introduction

Bone tissue possesses the ability to self-repair and regenerate; however, bone defects exceeding the critical size (typically defined as a defect length >1.5 times the diameter of the long bone) cannot recover unaided.[1] Bone tissue engineering scaffolds, designed

to temporarily fulfill the role of the extracellular matrix during new tissue regeneration, have attracted extensive attention for their potential in treating large bone defects.[2] Magnesium (Mg) and its alloys possess suitable mechanical properties, excellent biocompatibility, and ideal biodegradation.[3,4] Moreover, Mg^{2+} has been shown to promote osteogenesis and angiogenesis during bone regeneration.[5] Consequently, Mg alloys have been recognized as highly promising biomaterials for bone tissue engineering scaffolds.[6]

An ideal bone scaffold should feature an interconnected porous structure to support cell migration and nutrient transport.[7] Furthermore, high porosity and an appropriate pore size range (400–800 μm) can facilitate cell attachment and bone growth.[8] Traditional fabrication methods for Mg scaffolds, such as powder metallurgy, negative salt-pattern molding, and laser perforation, cannot reliably control pore morphology and distribution.[9] By contrast, laser powder bed fusion (L-PBF) offers clear advantages in fabricating porous scaffolds with complex internal structures and customized geometries at high precision, making L-PBF the preferred method for manufacturing porous Mg scaffolds.[10] However, L-PBF specimens cannot typically be used in the as-built state due to their high surface roughness. Surface treatment, therefore, is required to smooth scaffold surfaces, which is critical to enhance corrosion resistance and prevent fatigue failure.[11] For Mg scaffolds with intricate structures, L-PBF followed by electrochemical polishing has proven to be the most effective preparation route.[12]

The performance of porous Mg scaffolds is highly sensitive to formation defects and geometric deviations. Formation defects reduce scaffold mechanical properties and accelerate pitting corrosion during degradation.[13] Geometric deviations, in turn, compromise accurate performance evaluation by altering structural characteristics. With increasing porosity, the mechanical properties of porous scaffolds decrease exponentially, satisfying the Gibson-Ashby model.[11] Factors such as pore size, specific surface area, permeability, and gradient design also strongly influence the corrosion behavior and biological performance of porous scaffolds.[14,15] Across careful parameter optimization of L-PBF conditions, numerous studies have reported the successful fabrication of Mg scaffolds with high relative density.[16,17] However, geometric deviation has often been overlooked in prior research.

In L-PBF Mg scaffolds, substantial powder adhesion frequently occurs on down-facing surfaces, sometimes forming dross defects that decrease porosity and obstruct pores.[18] These deviations can be alleviated by polishing; however, if the deviations are too severe, polishing alone may not yield satisfactory results. For example, Xie *et al.*[19] fabricated Mg-neodymium (Nd)–zinc (Zn)–zirconium (Zr) scaffolds for antibacterial evaluation with a porosity of 32.1%. After polishing, porosity increased to 52.1%, which remained far below the designed value of 80%. Wang *et al.*[20] applied dynamic electropolishing to three types of L-PBF scaffolds. Although the resulting porosity values were only 1% lower than the design, radially graded pores emerged due to prolonged asymmetric polishing, and irregular protrusions caused by dross persisted. Therefore, reducing geometric deviations during the L-PBF process is critical to ensuring the dimensional accuracy of as-polished scaffolds.

Due to the high reactivity and low boiling point of Mg, the L-PBF process of Mg alloys often results in various microscale imperfections.[21] Compared to bulk samples, the processing window for achieving dense porous structures is narrower.[22] Liu *et al.*[23] fabricated WE43 scaffolds and found that relatively high energy input improved fusion quality but also caused increased powder adhesion and dimensional errors. Using a single L-PBF parameter thus presents a dilemma between achieving high fusion quality and maintaining high dimensional accuracy. In the contour area, the laser acts directly on the unconsolidated powder bed, where severe heat accumulation occurs, resulting in greater powder adhesion and dross defects.[24] Across multi-physics simulations, Wang *et al.*[22] discovered that a deeper molten pool formed during contour scanning and proposed that lower energy density should be applied at the edges. Similarly, Charles *et al.*[25] reported that reducing linear energy density near contour regions could suppress dross formation and dimensional deviations in inclined struts. For porous scaffolds with high specific surface area, contour formation accounts for a large proportion of the structure. Although these findings indicate that using low laser energy in contour scans can improve printing accuracy, research focusing specifically on this strategy remains inadequate, especially for high-precision porous Mg scaffolds.

In this study, we employed the novel biodegradable Mg-Nd-Zn-Zr alloy (JDBM) developed by our group, which has demonstrated excellent biocompatibility and corrosion resistance in both *in vitro* and *in vivo* investigations.[26,27] The aim was to prepare JDBM scaffolds with high formation quality and dimensional accuracy. An optimized L-PBF process was developed to reduce formation defects and geometric deviations by customizing energy input during contour scanning. The effectiveness of dynamic electrochemical polishing under different contour processes was compared, and the dimensional accuracy of the polished scaffolds was evaluated. Furthermore, the mechanical properties of the scaffolds were tested, and the experimental compressive strength was compared with finite element analysis (FEA) results.

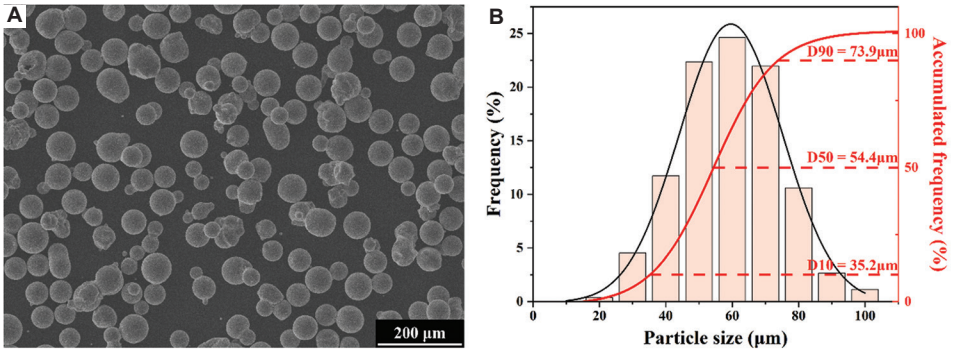

Figure 1. Characteristics of JDBM powders for laser powder bed fusion. (A) Scanning electron microscopy image of powder morphology. Scale bars: 200 μm; magnification: ×200. (B) Powder size distribution

2. Materials and methods

2.1. Materials

The JDBM alloy powder was prepared by centrifugal atomization (WHCA-40, Tangshan Weihao, China). As shown in Figure 1A, the particles were spherical and dense, with few satellite granules, indicating good powder quality. The particle size distribution, shown in Figure 1B, approximately followed a normal distribution. The statistical values for D10, D50, and D90 were 35.2 μm, 54.4 μm, and 73.9 μm, respectively. Table 1 presents the chemical composition of the powder and the L-PBF scaffolds, measured by inductively coupled plasma atomic emission spectroscopy (iCAP7600, Thermo, USA). The alloying element contents in the L-PBF scaffolds increased slightly, which may be attributed to the higher vaporization tendency of Mg during laser melting.

Table 1. Chemical composition of JDBM powder and laser powder bed fusion (L-PBF) scaffolds (wt.%)

Elements	Neodymium	Zinc	Zirconium	Magnesium
Powder	2.35	0.19	0.37	Balance
L-PBF scaffolds	2.74	0.19	0.39	Balance

2.2. Scaffold preparation

The pore topology of the scaffolds was defined using sheet gyroid units with a unit size of 2 mm, as shown in Figure 2A. Typically, a porosity of >70% is required for bone scaffolds.[28] Therefore, the target porosity was designed as 70%. The designed strut thickness and pore diameter were 210 μm and 800 μm, respectively. The porous scaffolds were fabricated using an L-PBF machine (iSLM160, ZRapid Tech, China) equipped with a laser spot diameter of 50 μm. The powder bed and Mg baseplate were pre-heated at 100°C for 1 h before printing. During printing, an inert atmosphere was maintained in the chamber with oxygen content below 200 ppm. Hatch spacing and layer thickness were set to 50 μm and 20 μm, respectively. Laser power (P) and scanning speed (V) were set in the ranges of 50–90 W and 200–600 mm/s, based on our previous work on JDBM cubes.[22] Figure 2B illustrates the scanning strategy, which involved contour scanning followed by filling for each layer. The offset distance (δ_C) between the contour line and filling line was set to 20 μm to ensure the effectiveness of contour scanning.[29] The scanning direction was rotated by 67° between adjacent layers.

After printing, the samples were removed from the baseplate and ultrasonically cleaned in 99 vol.% ethanol for 5 min. All samples were then subjected to dynamic electrochemical polishing until the porosity approached the designed value, using the apparatus shown in Figure 3A. The electrolyte consisted of 30 vol.% phosphoric acid and 70 vol.% C_2H_5OH. During polishing, the electrolyte temperature was maintained at 40°C, the voltage was set to 20 V, and the magnetic stirrer speed was 400 rpm. After polishing, the samples were cleaned in ethanol for 5 min to remove residual electrolytes.

2.3. Scaffold characterization

The formation quality of the L-PBF sample cross-sections was examined using optical microscopy (OM; Axio Observer A1, Zeiss, Germany). Relative density was calculated using ImageJ software (version 1.51; https://imagej.net/ij/). In ImageJ, OM images were converted to grayscale, and the thresholding tool was employed to determine the pore area fraction. Relative density was reported as the average of three different measurement regions. Surface morphology of the scaffolds was observed using scanning electron microscopy (SEM; VEGA 3 (LaB6); (TESCAN, Czech). Porosity was measured using the Archimedean method. Surface roughness was determined using a laser scanning confocal microscope (VK-X3000, KEYENCE, China). The internal structure was analyzed using an X-ray micro-computed tomography (micro-CT; Xradia 520 Versa,

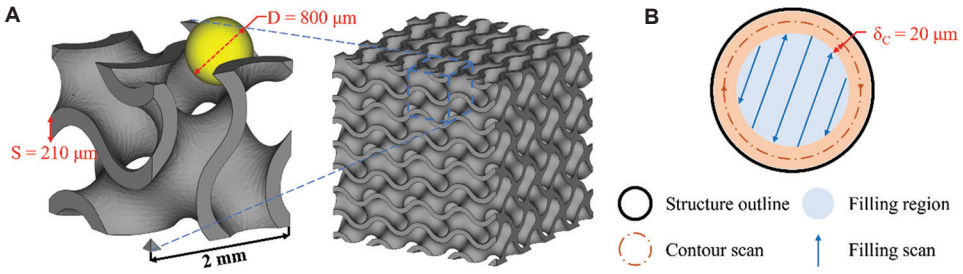

Figure 2. Design of the laser powder bed fusion process. (A) Gyroid unit cell and scaffold models. (B) Schematic of the scanning strategy

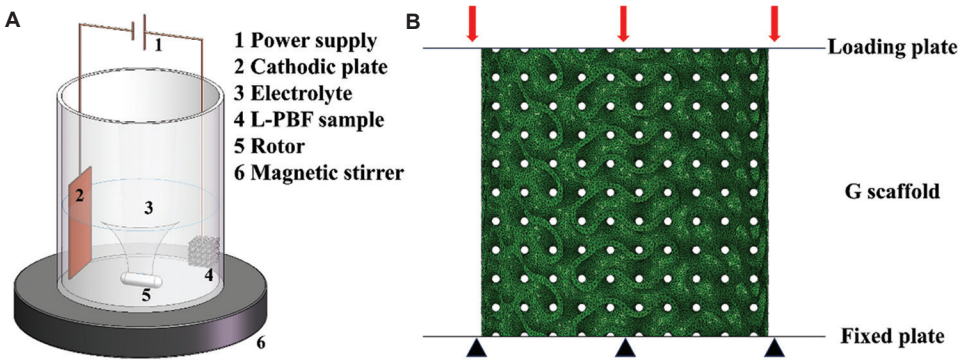

Figure 3. Experimental methods. (A) Schematic of the electrochemical polishing device. (B) Model setup for finite element analysis
Abbreviations: AM: Additively manufacture; G: Gyroid

Zeiss, Germany) at a resolution of 10 μm. The scanned data were imported into AvizoFire software (version 2019.1), Thermo Fisher Scientific, USA) for reconstruction. Geometric deviations of the reconstructed scaffold models were quantified based on the statistical distributions of the nearest neighbor distance between CT-derived point data and the design model surfaces, calculated using Materialise 3-matic software (version 11.0, Materialise, Belgium).

2.4. Mechanical testing

Compression tests were performed on cylindrical scaffolds (Ø10 × 10 mm) using a Zwick AG-100KN testing machine (ZwickRoell, Germany) at room temperature, at a crosshead speed of 1 mm/min, with three specimens tested for each condition.

FEA was conducted using Abaqus/Explicit (version 2022, Dassault Systèmes Simulia Corp., France) to investigate stress distribution. Scaffold models were meshed with C3D10M tetrahedral elements, with a grid size of 0.1 mm. Material properties were obtained from tensile tests on specimens fabricated under optimized parameters. The material was assumed to be homogeneous and isotropic, with an elastic modulus of 30.8 GPa and a Poisson's ratio of 0.35. The yield strength and ultimate tensile strength were 185 MPa and 252 MPa, respectively. Analysis steps were dynamic and explicit. Boundary conditions are shown in Figure 3B: The top plate was subjected to a displacement of 5 mm along the Z-axis, while the bottom plate was fixed.

3. Results and discussion

3.1. Formation quality

Figure 4A displays representative OM images of the cross-sections of porous scaffolds fabricated under different combinations of P and V. The linear energy density, P/V (J/mm), reflects the laser energy input. At high energy input, numerous large circular keyholes were observed (Figure 4A1). At low energy input, irregularly shaped lack-of-fusion defects appeared in two distribution patterns: (i) Uniformly distributed unfused cracks (Figure 4A4); and (ii) defects localized mainly at the central junction region, with fewer defects in the wall regions (Figure 4A3). At moderate energy input, relatively dense cross-sections with only a few small circular gas pores were observed (Figure 4A2). The relative density of these samples is presented in Figure 4C. The highest relative density of 99.44% was achieved at P = 80 W and V = 400 mm/s.

In L-PBF of Mg alloys, the primary defect types are lack-of-fusion defects and keyhole defects, both of which are closely linked to laser parameters.[28] Insufficient heat input leads to incomplete melting of the powder and

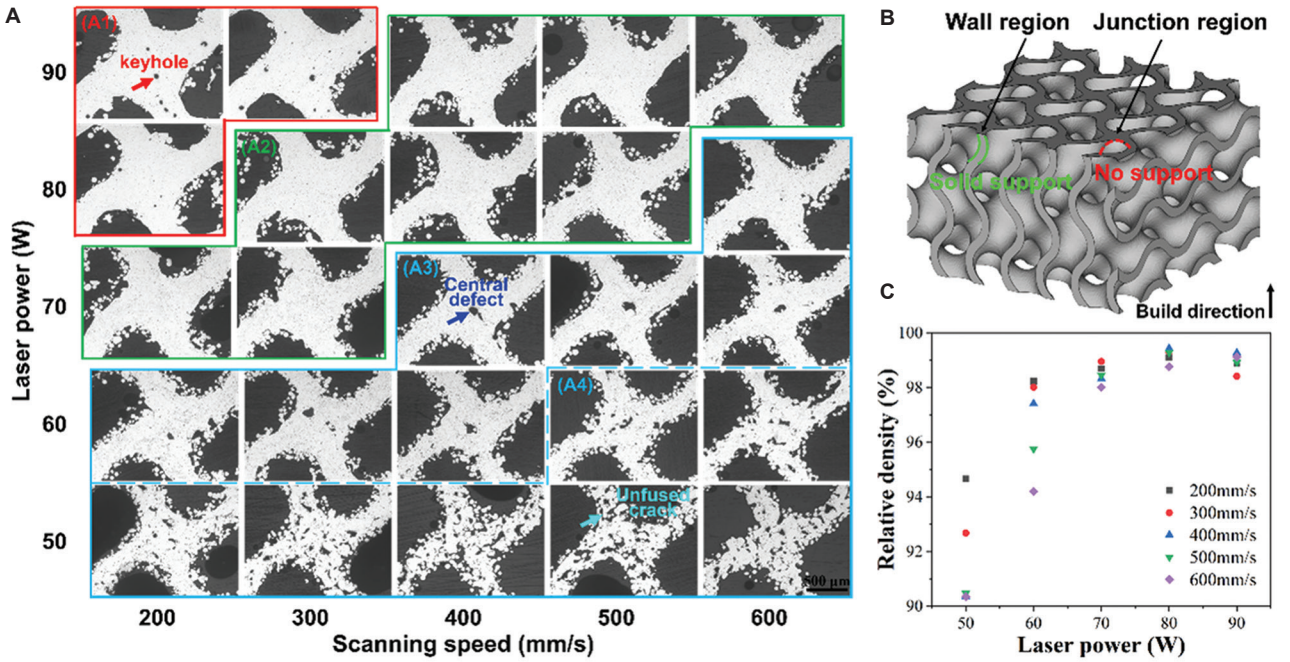

Figure 4. Fusion quality of porous scaffolds under various laser power and scanning speed. (A) Optical microscopy images of cross-sections at the junction region. Scale bars: 500 μm; magnification: ×50. (B) Typical regions of the porous structure. (C) Relative density

an unstable molten pool, ultimately causing elongated and sharp unfused cracks.[30] Increasing the energy input promotes complete melting and reduces crack defects, but central lack-of-fusion defects may persist. Considering the porous structure shown in Figure 4B, the junction region is located above the interconnected pores without effective support. During laser melting, the molten pool rests on loose powder, and under gravity, the bottom of the molten pool can deform or collapse, resulting in poor metallurgical bonding with adjacent tracks and the formation of central defects.[24] In addition, the thin junction regions consist of only a few slices in the design and lack sufficient interlayer remelting to eliminate central defects.[31] Therefore, for L-PBF porous scaffolds, structural factors also affect the manufacturability of specific regions and contribute to defect formation. At higher energy input, the remelting overlap between adjacent tracks expands, improving density in the junction regions. However, excessive heat input changes the molten pool from conduction mode to unstable keyhole mode.[32] A deep vapor cavity then forms, trapping gases within the solidified material and resulting in keyhole defects. Unlike lack-of-fusion or keyhole defects, the small gas pores observed in otherwise dense samples originate from gases dissolved in the melt or entrapped metal vapor, which are difficult to eliminate.[33] The high vaporization tendency of Mg exacerbates the formation of such pores.

Based on these results, P = 80 W and V = 400 mm/s were identified as optimal parameters for the filling scan. Unlike the filling region, the contour region tolerated a wider parameter range, as central defects were absent. Considering heat accumulation, lower laser power should be applied during contour scanning to reduce heat input. At P = 60 W, the laser energy was sufficient to form well-defined contours, whereas lower powers produced unfused cracks. Accordingly, four scanning strategies were designed to investigate the effects of contour scanning on formation quality: NCF84 (no contour scan, filling scan: 80 W/400 mm/s), C84F84 (both contour and filling scan: 80 W/400 mm/s), C64F64 (both contour and filling scan: 60 W/400 mm/s), and C64F84 (contour scan: 60 W/400 mm/s, filling scan: 80 W/400 mm/s).

As shown in Figure 5A, the top surfaces of all four scaffolds exhibited similar quality and structural accuracy, with only a few powder particles observed along the edges. In contrast, the side surfaces exhibited poorer quality due to extensive adhesion of unmelted powder (Figure 5B). Contour processing had a more significant influence on side surface morphology. In the NCF84 and C84F84 scaffolds, large powder agglomerates accumulated on the lower surfaces of the porous structures, forming dross that nearly blocked the pores. Powder adhesion and dross defects also increased sidewall thickness, resulting in significant structural deviations. By comparison, the C64F64 and C64F84 scaffolds exhibited more distinct pore structures, with fewer adhered particles and more consistent surface morphology. These results indicate that

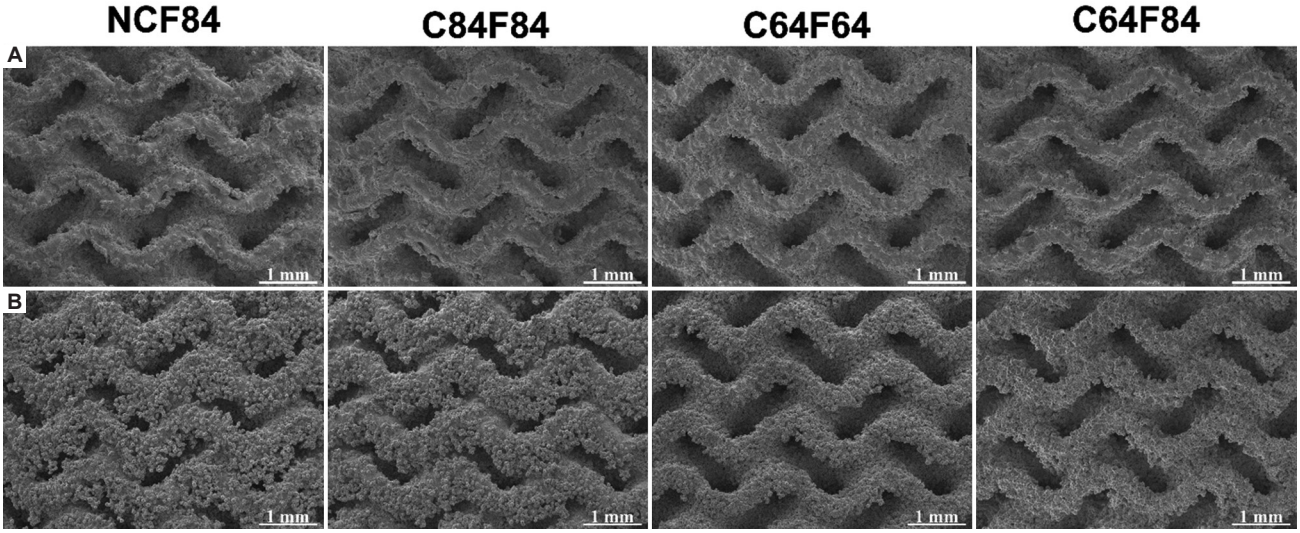

Figure 5. Scanning electron microscopy of the surface morphologies of scaffolds fabricated under four scanning strategies. (A)Top surfaces. (B) Side surfaces. Scale bars: 1 mm; magnification: ×50

powder adhesion and dross defects are strongly influenced by contour scan parameters.

The mechanism of dross formation is as follows: When the laser scan enters the powder region near an inclined solid edge, the low thermal conductivity of the loose powder causes the molten pool to overheat and transition to a keyhole-like mode. This produces a deeper depression in the powder bed and subsequent dross formation, referred to as the drilling effect.[34] Higher molten pool temperatures and slower cooling rates further promote partial melting and wetting of surrounding powder particles, increasing powder adhesion.[35] Reducing laser power during contour scanning is therefore an effective strategy to control powder adhesion and dross defects in porous scaffolds.

Figure 6A displays the CT-reconstructed models of the four scaffolds. The C64F84 and C64F64 scaffolds exhibited better geometric consistency with the design model at the macroscale. According to the CT cross-sectional images (Figure 6B), more residual powder particles were observed inside the cavities of the C84F84 and NCF84 scaffolds. For the C64F64 scaffold, contour scanning did not eliminate unfused defects in the junction regions. Analysis of the CT-reconstructed models revealed 9580, 7818, and 5043 gas pore defects in the NCF84, C84F84, and C64F84 scaffolds, respectively. The C64F84 scaffold contained fewer gas pores than the C84F84 and NCF84 scaffolds, likely because the lower-energy contour scan reduced the severe evaporation that occurs when the laser irradiates the powder bed. As shown in Figure 6C, in the longitudinal CT sections parallel to the printing direction, the NCF84 scaffold exhibited many protrusions and notches that compromised structural integrity. These side-surface defects were caused by the staircase effect resulting from distinct boundaries between adjacent layers.[36] Border melting introduced by contour scanning smoothed the surfaces and improved structural uniformity. For the C84F84 scaffolds, in addition to small powder particles, powder agglomerates were observed on the lower surfaces. In the C64F64 scaffold, unfused defects occurred at inclined struts instead of at the junction regions, confirming that defect location was related to porous structure geometry. Overall, the C64F84 scaffold exhibited the best formation quality and the least powder adhesion inside the structure.

Because the resolution of CT images was limited, Figure 7A presented OM cross-sectional images of the C64F84 scaffold, which showed a relative density of 99.54%. The circular gas pores had an average size of 5 μm. The porosities of the four scaffolds are shown in Figure 7B. Contour scanning with low laser power increased the porosity of the scaffolds. The average wall thickness, measured from the CT models, is shown in Figure 7C. With higher energy input, a larger contour region formed, which also led to greater dimensional deviations. Compared to the NCF84 scaffold, the wall thickness of the C64F84 scaffold decreased after applying a low-power contour scan. This was due to the single-digit percentage of laser absorptivity in solid bulk metals, which is much lower than that of the powder bed.[37] In the C64F84 scaffold, powder in the contour region melted into solid metal during the contour scan. In the subsequent filling scan, when the laser re-irradiated the contour region at the track endpoint, a smaller melt zone formed because of the reduced absorptivity of the solid.[38] Overall, high laser energy input increased molten pool size and improved fusion quality, while low laser

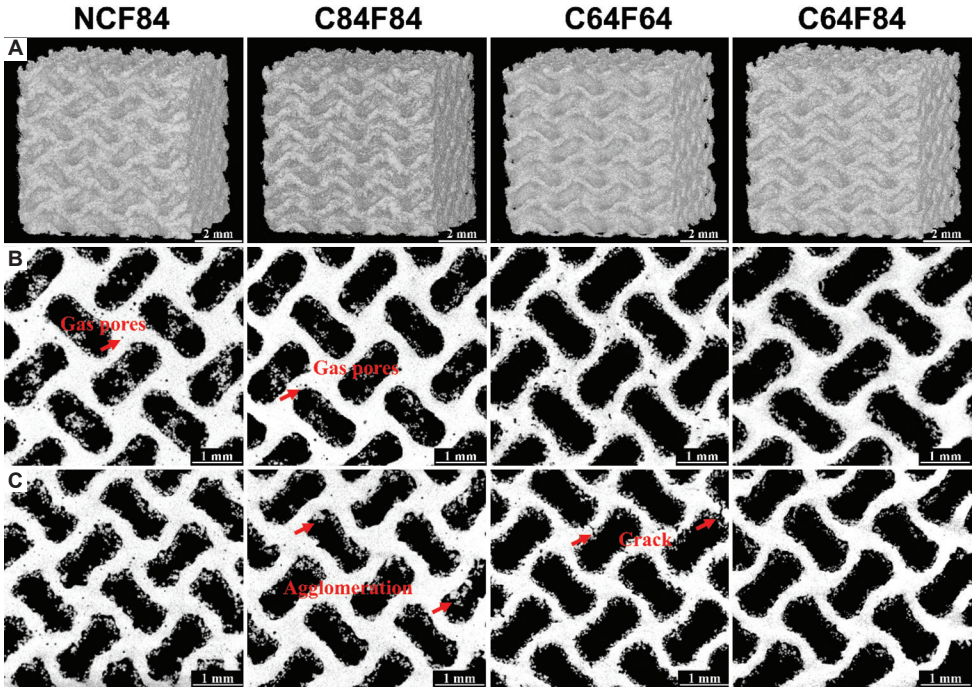

Figure 6. Formation quality of porous scaffolds under four scanning strategies. (A) Macroscopic computed tomography (CT)-reconstructed models. (B) Cross-sectional CT images. (C) Longitudinal CT images. Scale bars: (A) 2 mm, (B and C) 1 mm; magnification: A, B, and C 10 μm

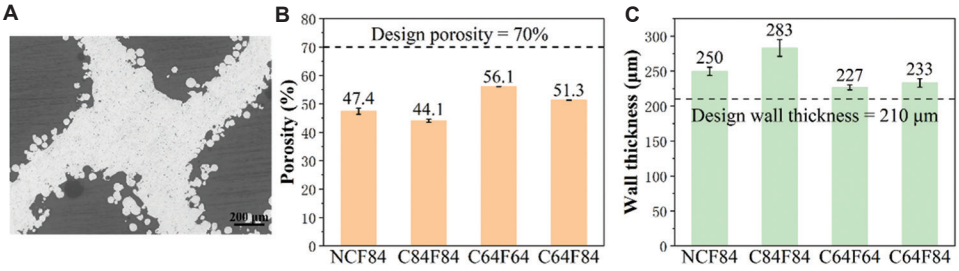

Figure 7. Characteristics of scaffolds. (A) Optical microscopy images of the C64F84 scaffold cross-section. Scale bars: 200 μm; magnification: ×50. (B) Porosity of porous scaffolds fabricated under four scanning strategies. (C) Wall thickness of porous scaffolds under four scanning strategies

energy input reduced powder adhesion and dross defects, thereby decreasing geometric deviation. Compared to the single-parameter strategies, the C64F84 strategy effectively combined the advantages of both processes.

3.2. Electrochemical polishing quality

To achieve smooth surfaces, the L-PBF scaffolds required electrochemical polishing. Based on fusion quality, the NCF84, C84F84, and C64F84 scaffolds were selected to compare polishing quality under different contour processes. Due to differences in porosity among the scaffolds, unequal polishing times were required. By monitoring porosity variation during polishing, the polishing times for the NCF84, C84F84, and C64F84 scaffolds were determined as 14, 20, and 10 min, respectively. After polishing, the porosity of all three scaffolds closely matched the design value of 70%, with a deviation of <0.5%.

As shown in Figure 8A, SEM images of the polished scaffolds revealed that most unmelted powder was removed, and the porous structures were clearly visible. For the NCF84 and C84F84 scaffolds, residual dross in solid form remained due to the lack of local targeting during polishing (Figure 8B). This finding underscores the need to minimize dross formation during the L-PBF process. The surface roughness (Sa) of the polished NCF84, C84F84, and C64F84 scaffolds was 22.8 μm, 11.4 μm, and 9.9 μm, respectively (Figure 8C). Electropolishing had a limited ability to improve surface roughness, and the initial surface roughness strongly influenced the final polished surface quality.[39] Incorporating contour scanning can reduce the surface roughness of L-PBF parts.[40]; accordingly, the C84F84 and C64F84

scaffolds exhibited lower surface roughness than the NCF84 scaffold after polishing. During polishing, surface roughness typically decreases rapidly at the beginning, following an exponential decay pattern similar to that of the material removal rate.[39] Larger geometric deviations significantly increased polishing inefficiency. Although the C84F84 scaffold required longer polishing than the C64F84 scaffold, both ultimately exhibited similar surface roughness.

To assess internal polishing quality, longitudinal CT images of the C84F84 and C64F84 scaffolds are shown in Figure 9A. The polishing process effectively removed residual powder within the scaffolds while also reducing wall thickness to a certain extent. The C84F84 scaffold retained some residual powder particles at its center and exhibited gradient structures. The wall thickness of the outer region was approximately 180 μm, whereas that of the inner region was approximately 260 μm, indicating uneven polishing. In comparison, the polished C64F84 scaffold displayed interconnected pores and relatively uniform wall thickness, with a measured pore size of 794.37 μm. CT-reconstructed models of the polished

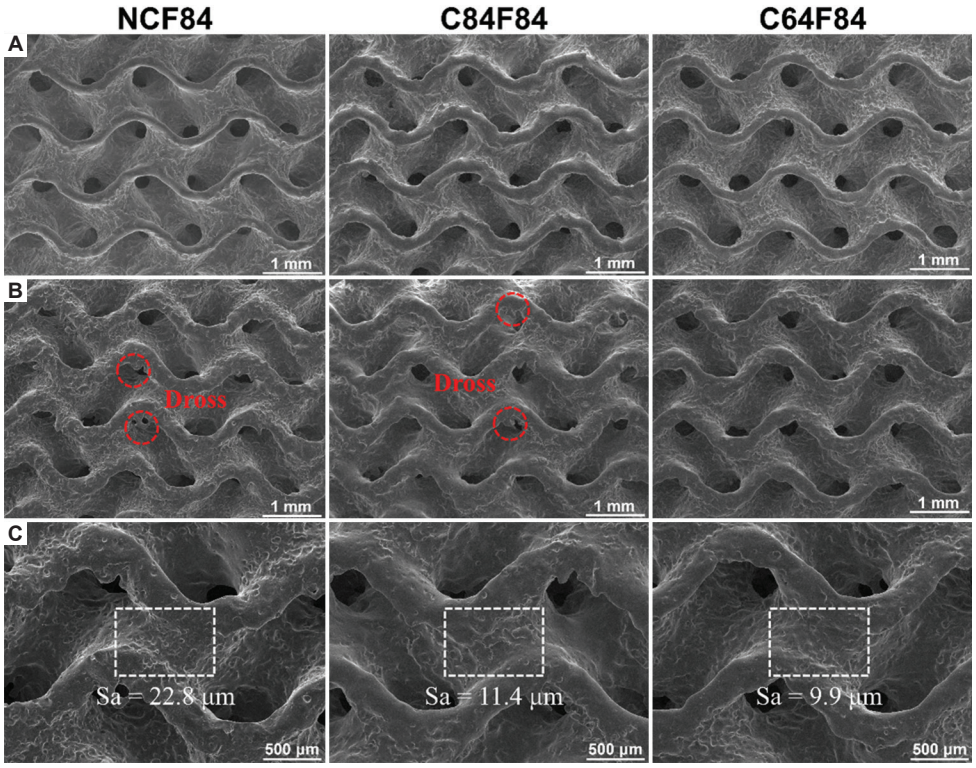

Figure 8. Scanning electron microscopy of the surface morphologies of the polished scaffolds under different contour processes. (A) Top surfaces. (B, C) Side surfaces. Scale bars: (A and B) 1 mm, (C) 500 μm; magnification: (A and B) ×50, (C) ×100

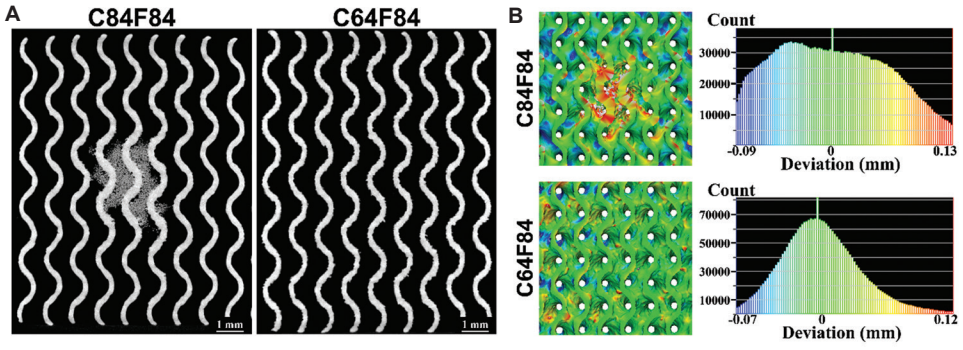

Figure 9. Polishing quality of the C84F84 and C64F84 scaffolds. Scale bars: 1 mm; magnification: 10 μm. (A) Longitudinal computed tomography images. (B) Three-dimensional deviation maps and corresponding histograms

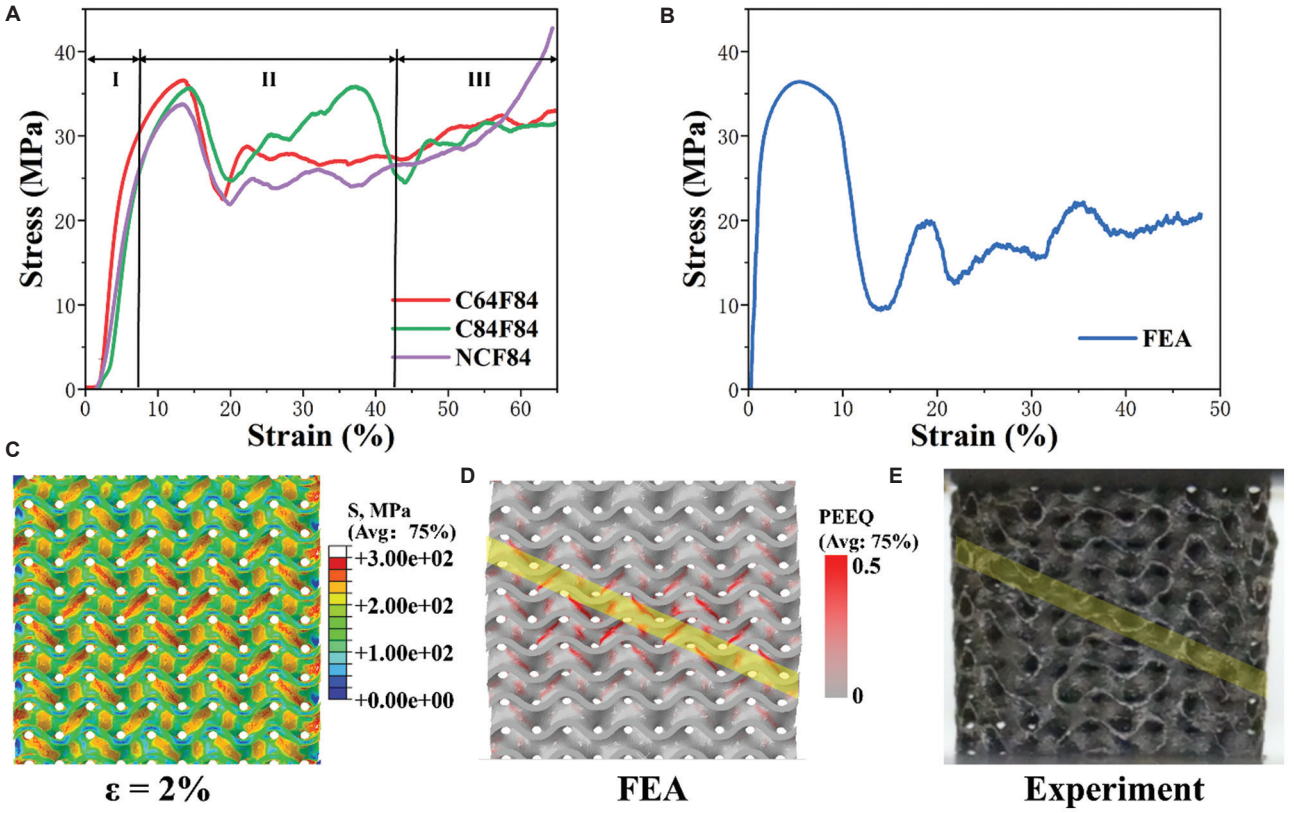

Figure 10. Mechanical properties of scaffolds. (A) Compression stress-strain curves. (B) Stress-strain curves predicted by finite element analysis (FEA). (C) Cross-sectional stress distribution predicted by FEA. (D) Cross-sectional plastic equivalent strain (PEEQ) nephogram predicted by FEA. (E) Compression deformation at the first stress peak

scaffolds were compared with the design model, and three-dimensional deviation maps were generated (Figure 9B). Red and blue regions indicate structural increasement and structural reduction, respectively. For the C84F84 scaffold, the internal structures showed more positive deviations, whereas the external structures showed negative deviations, confirming that polishing preferentially removed external material. For the C64F84 scaffold, the distribution of geometric deviations followed a Gaussian profile centered near zero. In contrast, the C84F84 scaffold displayed a higher proportion of large deviations, confirming the superior dimensional accuracy of the C64F84 scaffold. The mean deviation values for the C84F84 and C64F84 scaffolds were 0.008 mm and 0.003 mm, respectively, compared to 0.032 mm reported in previous studies.[20] These minor deviations aligned well with the measured porosity of 70%.

Electrochemical polishing is explained by the "viscous film theory": On rough surfaces, viscous films of different thickness and high electrical resistance form at protruding and recessed regions, resulting in higher dissolution rates at protrusions and eventual surface smoothing.[39] Because the electrolyte is fluid and flows into inner regions with stirring, electropolishing can treat both internal and external surfaces of porous scaffolds.[21] However, during the electropolishing of Mg, the electrolyte is consumed by reactions, and significant hydrogen gas evolves on the surface. For external regions, hydrogen gas readily dissipates into the solution, promoting electrolyte replenishment. For internal regions, however, hydrogen must diffuse through long pore channels, often coalescing into larger bubbles. These bubbles can block pores and hinder electrolyte flow, leading to insufficient replenishment and low local electrolyte density in inner regions.[20] Consequently, the dissolution rate inside the scaffold is slower than outside, generating uneven polishing. Prolonged polishing further aggravates this unevenness. In the C84F84 scaffolds, dross-blocked pores and narrower channels further inhibited dynamic electrolyte penetration, resulting in pronounced gradient structures. In contrast, the C64F84 scaffold exhibited better geometric consistency and required shorter polishing time, reducing asymmetry. Considering that polishing inevitably reduces wall thickness, a small positive geometric deviation is desirable in L-PBF scaffolds. Therefore, the C64F84 strategy proved to be the most suitable for preparing Mg scaffolds by L-PBF.

3.3. Mechanical properties

Cylindrical NCF84, C84F84, and C64F84 scaffolds were prepared for compression testing. Figure 10A displays the compressive stress–strain curves, which exhibited the three typical stages of porous structures: The elastic stage (I), the long plateau stage (II), and the densification stage (III). Compared to the NCF84 scaffold, the addition of contour scanning improved the compressive strength. Considering the small total volume of gas pores, formation defects were not the dominant factor accounting for strength differences among the scaffolds. With similar porosity, the enhanced strength can be attributed to higher damage tolerance resulting from improved surface quality and geometrical uniformity.[36] Due to strength variation across layers in the gradient structure, the C84F84 scaffold exhibited greater stress fluctuations. The C64F84 scaffold demonstrated the best mechanical performance, with an elastic modulus of 0.855 ± 0.017 GPa, a yield strength of 23.88 ± 0.72 MPa, and a compressive strength of 36.61 ± 0.19 MPa. These values match the mechanical properties of human cancellous bone, which has a compressive strength of 0.2–80.0 MPa and an elastic modulus of 0.01–2.00 GPa.[41] Thus, JDBM scaffolds could mitigate the stress shielding effect and support bone growth. The compressive strength calculated using FEA was 36.43 MPa (Figure 10B). The close agreement between the experimental and simulated results confirmed the high quality of the C64F84 scaffold. The cross-sectional von Mises stress distribution within the FEA models (Figure 10C) revealed that stress concentrations were primarily located in the junction regions and distributed diagonally, with more severe concentrations toward the center. Corresponding to this stress distribution, scaffolds failed by shear damage at the first stress peak. As shown in Figure 10D, shear bands were distinguishable in the cross-sectional plastic equivalent strain nephogram from FEA results. Similar shear bands were observed in the experimental results (Figure 10E).

4. Conclusion

This study investigated the fabrication of JDBM porous scaffolds with high formation quality and dimensional accuracy using the L-PBF process combined with electrochemical polishing. The main findings are summarized as follows:

(i) The optimal L-PBF parameters for the filling scan were P = 80 W and V = 400 mm/s. Contour scanning significantly influenced surface quality. Using low laser power for the contour scan reduced powder adhesion and dross defects on side surfaces, improving geometric consistency. With the optimal C64F84 scanning strategies, the relative density of L-PBF scaffolds reached 99.54%.

(ii) Electrochemical polishing effectively removed adhered powder particles from L-PBF scaffolds. However, different contour processes produced different polishing outcomes. Excessive polishing time and pore blockage caused uneven polishing between internal and external structures. Benefitting from the small positive geometric deviation of the L-PBF process, the polished C64F84 scaffolds exhibited higher dimensional accuracy and porosity consistent with the design value.

(iii) The C64F84 scaffold exhibited superior mechanical performance, with an elastic modulus of 0.855 GPa, a yield strength of 23.88 MPa, and a compressive strength of 36.61 MPa. Experimental compression results closely matched FEA predictions, confirming the high quality of the prepared JDBM scaffolds.

Acknowledgments

None.

Funding

This work was supported by the National Key Research and Development Program of China (No.2024YFB4610100, No.2024YFC2418602), the National Natural Science Foundation of China (No.52130104), Shanghai Jiao Tong University Medial-Engineering Cross Fund (YG2024LC05), the Scientific Research Foundation for Shenzhen high-level talents (No.RC2022-003), Guangdong Basic and Applied Basic Research Foundation (No.2022B1515120046), Sanming Project of Medicine in Shenzhen (No.SZSM202211038) and Shanghai Science and Technology Committee(23JC1402400).

Conflict of interest

The authors declare that they have no known competing financial interests or personal relationships that could have appeared to influence the work reported in this paper.

Author contributions

Conceptualization: Guangyin Yuan
Funding acquisition: Guangyin Yuan, Penghuai Fu, and Deli Wang
Investigation: Zeyu Feng, Hao Zheng, and Bozun Miao
Methodology: Zeyu Feng and Baoxue Zhou
Writing – original draft: Zeyu Feng
Writing – review and editing: Zeyu Feng, Guangyin Yuan, and Hua Huang

Ethics approval and consent to participate

Not applicable.

Consent for publication

Not applicable.

Availability of data

Data are available from the corresponding author on reasonable request.

References

1. Turnbull G, Clarke J, Picard F, *et al.* 3D bioactive composite scaffolds for bone tissue engineering. *Bioact Mater.* 2018;3(3):278-314.

   doi: 10.1016/j.bioactmat.2017.10.001

2. Koons GL, Diba ML, Mikos AG. Materials design for bone-tissue engineering. *Nat Rev Mater.* 2020;5(8):584-603.

   doi: 10.1038/s41578-020-0204-2

3. Chen Y, Xu Z, Smith C, Sankar J. Recent advances on the development of magnesium alloys for biodegradable implants. *Acta Biomater.* 2014;10(11):4561-4573.

   doi: 10.1016/j.actbio.2014.07.005

4. Shanmugavadivu A, Lekhavadhani S, Babu S, Suresh N, Selvamurugan N. Magnesium-incorporated biocomposite scaffolds: A novel frontier in bone tissue engineering. *J Magnesium Alloys*. 2024;12(6):2231-2248.

   doi: 10.1016/j.jma.2024.06.001

5. Xing F, Li S, Yin D, *et al.* Recent progress in Mg-based alloys as a novel bioabsorbable biomaterials for orthopedic applications. *J. Magnesium Alloys*. 2022;10(6):1428-1456.

   doi: 10.1016/j.jma.2022.02.013

6. Wang W, Jia G, Wang Q, *et al.* The *in vitro* and *in vivo* biological effects and osteogenic activity of novel biodegradable porous Mg alloy scaffolds. *Mater Des.* 2020;189:108514.

   doi: 10.1016/j.matdes.2020.108514

7. Alex Y, Vincent S, Divakaran N, *et al.* Pioneering bone regeneration: A review of cutting-edge scaffolds in tissue engineering. *Bioprinting*. 2024;43:e00364.

   doi: 10.1016/j.bprint.2024.e00364

8. Jia G, Huang H, Niu J, *et al.* Exploring the interconnectivity of biomimetic hierarchical porous Mg scaffolds for bone tissue engineering: Effects of pore size distribution on mechanical properties, degradation behavior and cell migration ability. *J Magnesium Alloys*. 2021;9(6):1954-1966.

   doi: 10.1016/j.jma.2021.02.001

9. Zheng YF, Gu XN, Witte F. Biodegradable metals. *Mater Sci Eng R Rep.* 2024;77:1-34.

   doi: 10.1016/j.mser.2014.01.001

10. Li Y, Jahr H, Zhou J, Zadpoor AA. Additively manufactured biodegradable porous metals. *Acta Biomater.* 2020;115:29-50.

    doi: 10.1016/j.actbio.2020.08.018

11. Sezer N, Evis Z, Koç M. Additive manufacturing of biodegradable magnesium implants and scaffolds: Review of the recent advances and research trends. *J Magnesium Alloys*. 2021;9(2):392-415.

    doi: 10.1016/j.jma.2020.09.014

12. Pourrahimi S, Hof LA. On the post-processing of complex additive manufactured metallic parts: A review. *Adv Eng Mater.* 2024;26(10):2301511.

    doi: 10.1002/adem.202301511

13. Niu X, Shen H, Fu J, *et al.* Corrosion behaviour of laser powder bed fused bulk pure magnesium in hank's solution. *Corros Sci.* 2019;157:284-294.

    doi: 10.1016/j.corsci.2019.05.026

14. Peng B, Xu H, Song F, *et al.* Additive manufacturing of porous magnesium alloys for biodegradable orthopedic implants: Process, design, and modification. *J Mater Sci Technol.* 2024;182:79-110.

    doi: 10.1016/j.jmst.2023.08.072

15. Qin Y, Wen P, Guo H, *et al.* Additive manufacturing of biodegradable metals: Current research status and future perspectives. *Acta Biomater.* 2019;98:3-22.

    doi: 10.1016/j.actbio.2019.04.046

16. Yin B, Liu J, Peng B, *et al.* Influence of layer thickness on formation quality, microstructure, mechanical properties, and corrosion resistance of WE43 magnesium alloy fabricated by laser powder bed fusion. *J Magnesium Alloys*. 2024;12(4):1367-1385.

    doi: 10.1016/j.jma.2022.09.016

17. Li K, Ji C, Bai S, *et al.* Selective laser melting of magnesium alloys: Necessity, formability, performance, optimization and applications. *J Mater Sci Technol.* 2023;154:65-93.

    doi: 10.1016/j.jmst.2022.12.053

18. Sadat Hashemi T, Jaiswal S, McCarthy HO, Levingstone TJ, Dunne NJ. Biofunctionalisation of porous additively manufactured magnesium-based alloys for Orthopaedic applications: A review. *Biomater Adv.* 2025;169:214170.

    doi: 10.1016/j.bioadv.2024.214170

19. Xie K, Wang N, Guo Y, *et al.* Additively manufactured biodegradable porous magnesium implants for elimination of implant-related infections: An *in vitro* and *in vivo* study. *Bioact Mater.* 2021;8:140-152.

    doi: 10.1016/j.bioactmat.2021.06.032

20. Wang Y, Huang H, Jia G, Zeng H, Yuan G. Fatigue and dynamic biodegradation behavior of additively manufactured Mg scaffolds. *Acta Biomater.* 2021;135:705-722.

    doi: 10.sci1016/j.actbio.2021.08.040

21. Ansari N, Alabtah FG, Albakri MI, Khraisheh M. Post

processing of additive manufactured Mg alloys: Current status, challenges, and opportunities. *J Magnesium Alloys*. 2024;12(4):1283-1310.

doi: 10.1016/j.jma.2024.04.017

22. Wang Y, Wang L, Liu D, *et al.* Mechanisms of processing map difference between laser powder bed fusion of Mg solid cubes and lattice structures. *Addit Manuf.* 2023;76:103773.

doi: 10.1016/j.addma.2023.103773

23. Liu J, Liu B, Min S, *et al.* Biodegradable magnesium alloy WE43 porous scaffolds fabricated by laser powder bed fusion for orthopedic applications: Process optimization, *in vitro* and *in vivo* investigation. *Bioact Mater.* 2022;16:301-319.

doi: 10.1016/j.bioactmat.2022.02.020

24. Chen H, Gu D, Xiong J, *et al.* Improving additive manufacturing processability of hard-to-process overhanging structure by selective laser melting. *J Mater Process Technol.* 2017;250:99-108.

doi: 10.1016/j.jmatprotec.2017.06.044

25. Charles A, Bayat M, Elkaseer A, *et al.* Elucidation of dross formation in laser powder bed fusion at down-facing surfaces: Phenomenon-oriented multiphysics simulation and experimental validation. *Addit Manuf.* 2022;50:102551.

doi: 10.1016/j.addma.2021.102551

26. Qin H, Zhao Y, An Z, *et al.* Enhanced antibacterial properties, biocompatibility, and corrosion resistance of degradable Mg-Nd-Zn-Zr alloy. *Biomaterials*. 2015;53:211-220.

doi: 10.1016/j.biomaterials.2015.02.096

27. Xie K, Wang L, Guo Y, *et al.* Effectiveness and safety of biodegradable Mg-Nd-Zn-Zr alloy screws for the treatment of medial malleolar fractures. *J Orthop Transl.* 2021;27:96-100.

doi: 10.1016/j.jot.2020.11.007

28. Xuehua W, Junying L, Youwen Y, *et al.* Laser powder bed fusion of biodegradable magnesium alloys: Process, microstructure and properties. *Int J Extreme Manuf.* 2025;7(2):022007.

doi: 10.1088/2631-7990/ad967e

29. Tan C, Li S, Essa K, *et al.* Laser Powder Bed Fusion of Ti-rich TiNi lattice structures: Process optimisation, geometrical integrity, and phase transformations. *Int J Mach Tools Manuf.* 2019;141:19-29.

doi: 10.1016/j.ijmachtools.2019.04.002

30. Kasperovich G, Haubrich J, Gussone J, *et al.* Correlation between porosity and processing parameters in TiAl6V4 produced by selective laser melting. *Mater Des.* 2016;105:160-170.

doi: 10.1016/j.matdes.2016.05.070

31. Zhang C, Zheng H, Yang L, *et al.* Mechanical responses of sheet-based gyroid-type triply periodic minimal surface lattice structures fabricated using selective laser melting. *Mater Des.* 2022;214:110407.

doi: 10.1016/j.matdes.2022.110407

32. Snow Z, Nassar AR, Reutzel EW. Invited Review Article: Review of the formation and impact of flaws in powder bed fusion additive manufacturing. *Addit Manuf.* 2020;36:101457.

doi: 10.1016/j.addma.2020.101457

33. Wei HL, Mukherjee T, Zhang W, *et al.* Mechanistic models for additive manufacturing of metallic components. *Prog Mater Sci.* 2021;116:100703.

doi: 10.1016/j.pmatsci.2020.100703

34. Hussain A, Kim D. Fabrication of metal alloy structures with overhang features in laser-based powder bed fusion: A critical review of challenges and latest developments. *J Manuf Processes*. 2025;135:112-130.

doi: 10.1016/j.jmapro.2025.01.031

35. Carter LN, Villapún VM, Grover L, *et al.* Exploring the duality of powder adhesion and underlying surface roughness in laser powder bed fusion processed Ti-6Al-4V. *J Manuf Processes*. 2022;81:14-26.

doi: 10.1016/j.jmapro.2022.06.057

36. Huang L, Wan H, Han Q, *et al.* Mitigating surface notches for enhanced fatigue performance of metallic gyroid structures via contour scanning. *Int J Mech Sci.* 2025;286:109913.

doi: 10.1016/j.ijmecsci.2024.109913

37. Liu J, Wen P. Metal vaporization and its influence during laser powder bed fusion process. *Mater Des.* 2022;215:110505.

doi: 10.1016/j.matdes.2022.110505

38. Ren Z, Wei D, Wang S, Zhang DZ, Mao S. On the role of pre- and post-contour scanning in laser powder bed fusion: Thermal-fluid dynamics and laser reflections. *Int J Mech Sci.* 2022;226:107389.

doi: 10.1016/j.ijmecsci.2022.107389

39. Han W, Fang F. Fundamental aspects and recent developments in electropolishing. *Int J Mach Tools Manuf.* 2019;139:1-23.

doi: 10.1016/j.ijmachtools.2019.01.001

40. Maleki E, Salehnasab B, Paul M, Shao S, Shamsaei N. Dimensional accuracy of fabricated geometries through powder bed fusion: An overview and a new benchmark artifact proposal. *Mater Des.* 2025;114361.

doi: 10.1016/j.matdes.2025.114361

41. Wang Y, Fu P, Wang N, *et al.* Challenges and solutions for the additive manufacturing of biodegradable magnesium implants. *Engineering*. 2020;6(11):1267-1275.

doi: 10.1016/j.eng.2020.02.015